Sound & Vibration 2026, 60(5), 4403.
doi: https://doi.org/10.59400/sv4403

Article

Modeling and simulation of hybrid electric propulsion systems for amphibious vehicle

Van-Tong Em Nguyen[1,2], Van-Trang Nguyen[1,*], Tat-Hien Le[3,4], Cao-Thanh Nhi Ninh[1], Thai-Nguyen Vo[2]

[1] Faculty of Energy Engineering and Transport, Ho Chi Minh City University of Technology and Engineering (HCM-UTE), Ho Chi Minh City 700000, Vietnam

[2] College of Engineering and Technology, Nam Can Tho University (DNC), Can Tho City 94000, Vietnam

[3] Faculty of Transportation Engineering, Ho Chi Minh City University of Technology (HCMUT), Ho Chi Minh City 700000, Vietnam

[4] Vietnam National University Ho Chi Minh City (VNU-HCM), Ho Chi Minh City 700000, Vietnam

*** Corresponding author:** Van-Trang Nguyen, trangnv@hcmute.edu.vn

CITATION

Nguyen VTE, Nguyen VT, Le TH, et al. Modeling and simulation of hybrid electric propulsion systems for amphibious vehicle. Sound & Vibration. 2026; 60(5): 4403. https://doi.org/10.59400/sv4403

ARTICLE INFO

Received: 15 May 2026
Revised: 28 June 2026
Accepted: 7 July 2026
Available online: 26 July 2026

Abstract: Amphibious vehicles operate across land and water, requiring stable environmental transitions. Although series hybrid electric propulsion systems (Series HEPS) offer flexible power distribution for these dual-environment demands, existing studies often limit dynamic analysis to individual environments. The transition phase, where buoyancy, hydrodynamic drag, and wheel loads vary simultaneously, lacks a unified mathematical framework. This study develops an integrated longitudinal dynamic model coupled with a Series HEPS, enabling continuous simulation across three phases: land, water, and transition. The land phase considers rolling resistance, aerodynamic drag, and wheel traction, whereas the water phase determines hydrodynamic resistance via the Holtrop-Mennen method and a propeller thrust model. Notably, for the transition phase, a proposed geometric relationship links longitudinal displacement along the bank slope to submergence depth, determining real-time buoyancy variations and wheel load redistribution. Simulation scenarios evaluate velocity, acceleration, and traction requirements across all phases, analyzing the influence of bank slope angles and ground friction on climbing capability. Simulation results demonstrate that the proposed HEPS configuration is highly reliable, achieving maximum speeds of 60 km/h on land and over 8 km/h in water. The system effectively satisfies the dynamic performance requirements, including velocity, acceleration, and gradeability, across the terrestrial, aquatic, and transitional phases. The simulation results indicate that the proposed HEPS configuration provides continuous tractive effort across the operating phases, achieving the required on-road design speed of 60 km/h, reaching approximately 8.7 km/h in calm-water operation, and attaining terminal transition velocities of approximately 7.2–9.5 km/h during the aquatic-to-terrestrial transition. This framework provides a useful analytical tool for the preliminary design and dynamic evaluation of hybrid amphibious vehicles.

Keywords: amphibious vehicle; series hybrid electric propulsion; longitudinal dynamic modelling; environment transition phase; power distribution

1. Introduction

The transportation sector is a major contributor to global greenhouse gas emissions, prompting a critical shift toward sustainable and efficient alternative propulsion solutions [1–3]. Among the technologies being deployed, Hybrid Electric Vehicles (HEVs) are considered a feasible transitional solution between conventional internal combustion engine vehicles and Battery Electric Vehicles (BEVs) [4].

In this context, the extended-range Series Hybrid Electric Propulsion System (Series HEPS) has emerged as a solution that balances operational efficiency and flexibility [5, 6]. This system operates similarly to a BEV, in which the electric motor provides the primary traction and the battery serves as the main energy source [4]. Unlike a pure BEV, the extended-range configuration incorporates an internal combustion engine coupled with a generator to maintain the battery state of charge when the energy level drops below a predefined threshold, thereby ensuring continuous operation and extending the driving range [7–10]. This characteristic is particularly suitable for vehicles that require high maneuverability and operation under diverse environmental conditions, such as amphibious vehicles that must transition seamlessly between land and water surfaces [11–15].

The need for trans-media operation, or continuous transportation between aquatic and terrestrial settings, makes the technical problem for an amphibious vehicle much more complicated. While tire traction and terramechanics interactions control mobility on land, buoyancy and hydrodynamic drag control motion in the aquatic environment. Several studies have tackled this issue from the standpoint of modeling the interaction between the environment and the vehicle. To simulate vehicle motion in the surf zone under complicated terrain conditions, Yamashita et al. [16] created a model that combines computational fluid dynamics (CFD) with multi-body dynamics (MBD). To assess the water ingress process and set safety standards, Burciu et al. [17] used a RANSE model in conjunction with towing tank trials. In order to increase stability during the transition from water to land, Huang et al. [18] concentrated on a traction control approach based on Burckhardt data. Tison [19] used multiphase CFD in conjunction with a six-degree-of-freedom (6-DOF) model to examine dynamic features under different operating conditions. In order to assess the impact of velocity and water exit angle on transition performance, Liu et al. [20] used a RANS model with Bekker theory.

Although the aforementioned studies have achieved high accuracy in describing hydro-aerodynamic interactions and multi-degree-of-freedom motion, a significant research gap still exists. First, the propulsion system of the vehicle is often treated as an ideal traction source or a fixed input parameter, and has not been directly integrated into the dynamic equations throughout the trans-media process. Second, most studies analyze the aquatic and on-land states separately, whereas the transition phase, where buoyancy gradually decreases, hydrodynamic drag diminishes, and mechanical resistance increases simultaneously is the most nonlinear and sensitive stage with respect to operational stability. Third, CFD–MBD models provide high accuracy but incur high computational cost, which limits their applicability in preliminary design optimization or parametric analysis under real terrain conditions such as soft soil or muddy environments.

Motivated by the foregoing limitations, the present study proposes an integrated modeling and simulation framework for a Series Hybrid Electric Propulsion System

(Series HEPS) applied to an amphibious vehicle. The principal novelties and contributions of this work are summarized as follows. First, unlike prior studies that treat the propulsion system as an ideal traction source decoupled from the vehicle's environmental interaction, the proposed framework directly embeds the electric motor torque characteristics, gear-ratio mapping, and power-flow constraints into the longitudinal equations of motion across all three operating phases (on-land, in-water, and transition), yielding a fully coupled propulsion–dynamics model. Second, a closed-form geometric relationship is derived that analytically links the instantaneous draft, the waterline contact length, and the longitudinal displacement through the bank slope angle, enabling real-time computation of buoyancy variation and normal wheel-load redistribution during the aquatic-to-terrestrial transition without requiring computationally expensive CFD iterations. Third, the entire framework is implemented as a single MATLAB/Simulink simulation environment that continuously resolves the force and moment equilibrium across the three phases, allowing direct parametric sensitivity analysis with respect to bank slope angle, payload, and friction coefficient, a capability that is absent in existing phase-separated models. These methodological contributions collectively advance the state of the art by providing a computationally efficient yet physically consistent analytical tool suitable for the preliminary design and dynamic evaluation of hybrid amphibious vehicles with low emissions and high operational adaptability.

To further emphasize the theoretical novelty of Huang et al. [18], the proposed framework differs from existing coupled methods such as CFD–MBD [16], RANSE [17], multiphase CFD–6DOF [20], and RANS–terramechanics models [19], which mainly focus on high-fidelity fluid–structure or terrain–vehicle interactions and usually require substantial computational effort. In these models, the propulsion system is often simplified as an ideal traction source or prescribed input. By contrast, Huang et al. [18] introduce an analytical order-reduced formulation in which the water-to-land transition is described through a closed-form geometric projection model [21] relating instantaneous draft, waterline length, and longitudinal displacement along the bank slope. This enables the hydrodynamic resistance decay and mechanical grade-resistance growth to be continuously coupled with the torque–power characteristics and operating limits of the electric motor. Thus, the framework provides a unified differential-equation model for evaluating powertrain dynamics across land, water, and transition phases with improved computational efficiency.

2. Research methodology

The system-oriented dynamic modeling approach used in this study consists of the following primary steps: (1) determining the amphibious vehicle's propulsion system configuration and operational requirements; (2) establishing the vehicle's basic design parameters; (3) creating dynamic mathematical models for three operating phases: on-land, in-water, and during transition; and (4) running numerical simulations to assess dynamic characteristics under various operating scenarios. This method makes it possible to create a single analytical framework that is appropriate for preliminary design review and guarantees physical consistency across various operating settings.

2.1. Propulsion system architecture and overall vehicle layout

The layout of system components is optimized laterally to preserve the vehicle's overall balance as well as longitudinally to guarantee dynamic stability in both operating scenarios. To maximize load distribution between the front and back axles, the battery pack is placed close to the middle of the car chassis in the longitudinal direction. In order to preserve total load balance and contribute to stability during in-water operation, the ICE and generator are positioned at the back. Major parts such the battery pack, electric motor, and power conversion system are symmetrically positioned around the longitudinal center plane of the vehicle in the lateral orientation. When the vehicle is operating in water or on uneven terrain, this symmetry reduces roll moments caused by buoyancy variations and limits sideways tilting by bringing the center of gravity (CG) closer to the longitudinal centerline.

The fundamental design parameters of the amphibious vehicle, summarized in **Table 1**, are systematically determined based on the operational requirements of a light-duty, 4-passenger vehicle intended for ecotourism in calm inland waterways and littoral zones. The dimensional specifications (overall length, width, and ground clearance) and mass distribution are benchmarked against existing commercial recreational amphibious platforms to ensure spatial feasibility and stable hydrostatics. The gross vehicle mass (860 kg) is explicitly calculated by aggregating the curb weight (600 kg) with the payload of four adult occupants (65 kg/person). Furthermore, based on preliminary longitudinal dynamic calculations, the nominal capacity of the electric traction motor is sized at 7.5 kW. This power rating is specifically selected to provide a sufficient safety margin over the peak power demand (approximately 7.475 kW) required to overcome the maximum coupled hydro-mechanical resistance during the critical aquatic-to-terrestrial transition phase on a 20° incline.

Table 1. Basic design specifications of the amphibious vehicle.

Parameters	Values
Overall length, L (mm)	4,432
Overall width, W (mm)	1,754
Overall height, H (mm)	1,361
Wheelbase, L_{wb} (mm)	2,391
Track width, T (mm)	1,351
Ground clearance, h_c (mm)	184
Curb weight, m_0 (kg)	600
Gross vehicle mass, m (kg)	860
Front axle load, m_f (kg)	412.8
Rear axle load, m_r (kg)	447.2
Number of occupants (including driver), n_p	4
Passenger mass per person, m_p (kg)	65
Design speed on road, v_{road} (km/h)	60
Design speed in water, v_{river} (km/h)	8–9
Drivetrain configuration	4 × 2

As illustrated in **Figure 1**, for optimal load balance and amphibious stability, the internal combustion engine (ICE) and generator are front-mounted, while the core powertrain components, including battery pack, electric motor, and power converters, are symmetrically aligned along the longitudinal axis. This configuration centralizes the center of gravity (CG), significantly mitigating buoyancy-induced roll moments and lateral tilt across uneven or aquatic terrains. Furthermore, power flow within this series hybrid electric propulsion system (HEPS) is regulated by a thermostat-based Energy Management Strategy (EMS). To isolate the ICE-generator from transient load fluctuations, the battery exclusively fulfills propulsion demands while its state of charge (SOC) remains above a critical threshold. Upon reaching a predefined lower SOC limit, the engine activates strictly at its optimal brake specific fuel consumption (BSFC) point, supplying constant power for simultaneous propulsion and recharging until the upper SOC target is achieved. While this foundational rule-based logic ensures continuous power delivery and operational stability for the dynamic performance simulations conducted in this study, the development and integration of advanced, optimization-based energy management algorithms are reserved for subsequent research phases.

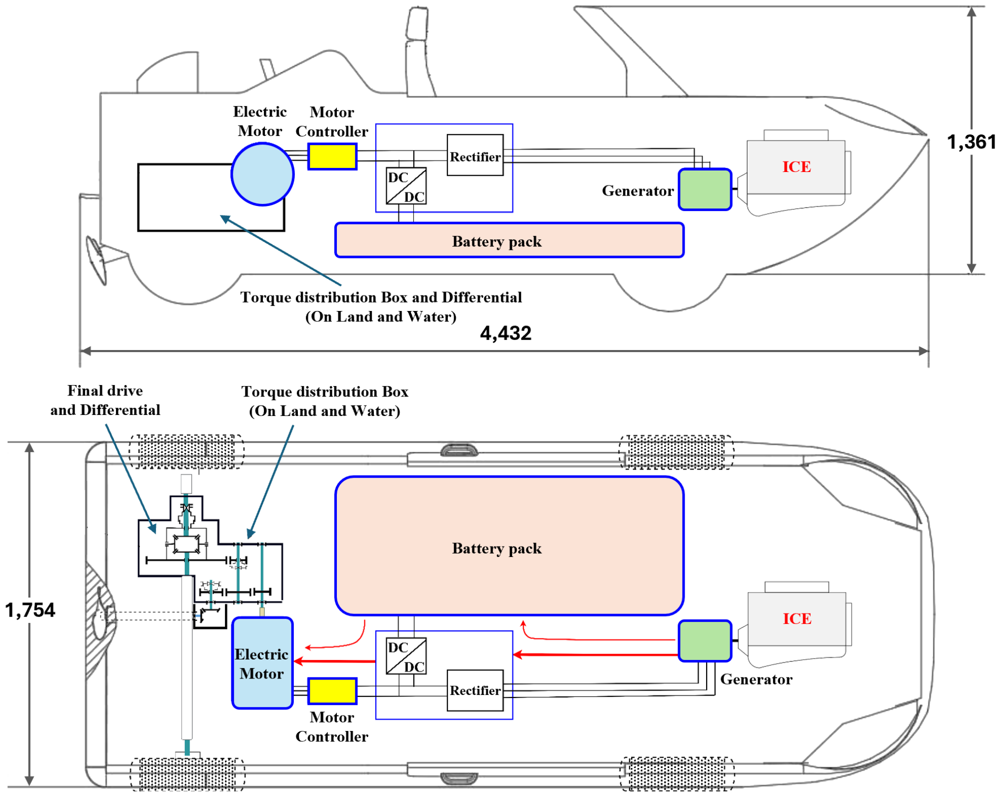

Figure 1. Overall layout of hybrid electric propulsion systems for amphibious vehicles.

2.2. Longitudinal dynamic model of the amphibious vehicle in on-land operation

In the on-land operating mode, the amphibious vehicle is modeled as a one-dimensional dynamic system moving along the longitudinal direction. It is assumed that the vehicle has a total mass m, moving with an instantaneous velocity v and acceleration a. The general case considered is the vehicle ascending a slope with an incline angle α. The forces acting on the vehicle under these conditions are illustrated in **Figure 2**, including the traction force at the driven wheels and the components of resistive forces. According to the longitudinal dynamic equilibrium principle, the tangential traction force F_k at the driven wheels is used to overcome the following resistive forces: rolling resistance (F_f), slope resistance (F_i), aerodynamic drag (F_w), and inertial force (F_j) [22,23].

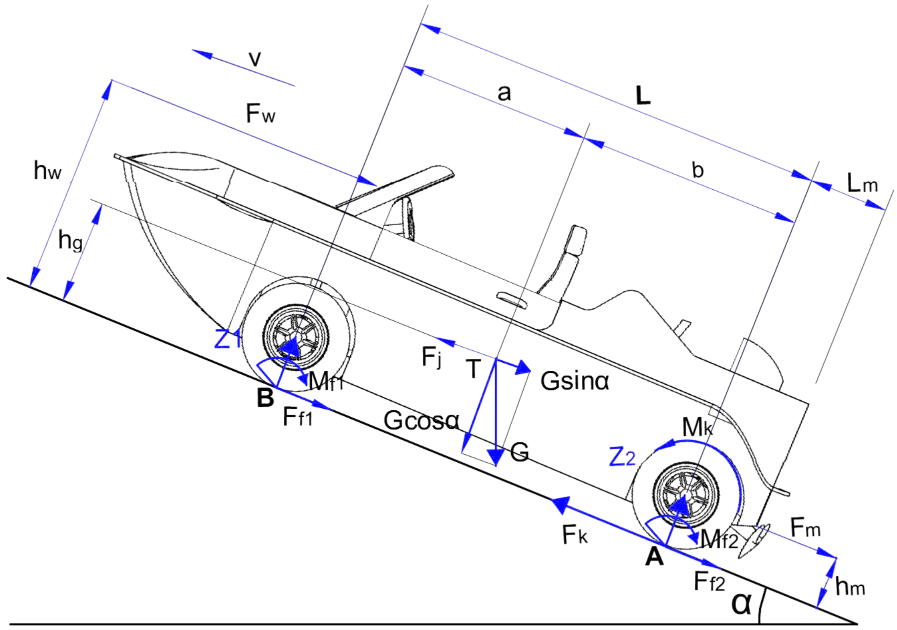

Figure 2. Forces and moments acting on the amphibious vehicle during uphill on-land motion.

Longitudinal traction force equilibrium equation of the amphibious vehicle on an uphill slope (on land):

$$F_k = F_f + F_W + F_i + F_j \tag{1}$$

$$F_k = mgf \cdot cos\alpha + \frac{1}{2}\rho AC_d v^2 + G \cdot sin\alpha + ma + I \cdot \frac{G_l^2}{n_g r^2} a \tag{2}$$

where g is the gravitational acceleration (m/s²); f is the rolling resistance coefficient; aerodynamic parameters include ρ, the air density (kg/m^3), A, the frontal area (m^2), and C_d, the aerodynamic drag coefficient. Typically, the motor's moment of inertia is not explicitly determined. Therefore, an approximate calculation is to increase the vehicle mass by 5% in Equation (2) and neglect the term $I \cdot \frac{G_l^2}{n_g \cdot r^2} \cdot a$ to account for the effects of rotating masses [23].

Based on the overall propulsion system layout of the Amphibious Vehicle proposed in this study (**Figure 1**).

When the amphibious vehicle operates on a horizontal road, with an air density of 1.25 kg·m^{-3}, the equation is given as:

$$\begin{gathered} F_k = mgf \cdot cos\alpha + \tfrac{1}{2}\rho AC_d v^2 + G \cdot sin\alpha + ma + I \cdot \tfrac{G_l^2}{n_g r^2} a \tfrac{G_l}{r} T_m = \\ mgf + \tfrac{1}{2}\rho AC_d v^2 + \left(m + I\tfrac{G_l^2}{n_g r^2}\right)\tfrac{dv}{dt} \end{gathered} \tag{3}$$

where T_m is the torque of the electric motor; G_l is the gear ratio of the power transmission system connecting the electric motor to the driven wheel axle; and r is the wheel radius.

In the initial stage, when the electric motor torque is constant, Equation (3) yields:

$$\frac{dv}{dt} = \frac{n_t \frac{G_l}{r} T_{m,max} - mgf}{m + I\frac{G_l^2}{n_g r^2}} - \frac{\frac{1}{2}\rho A C_d v^2}{m + I\frac{G_l^2}{n_g r^2}} \tag{4}$$

This equation remains valid until the torque begins to decrease, i.e., when $\omega \geq \omega_c$ or $v \geq \left(\frac{r}{G_l}\right)\omega_c$, at which point the power remains constant and the torque decreases hyperbolically as the electric motor speed increases. From Equation (4), the velocity is governed by the following differential equation:

$$\frac{dv}{dt} = \frac{n_t \frac{P_E}{v}}{m + I\frac{G_l^2}{n_g r^2}} - \frac{mgf}{m + I\frac{G_l^2}{n_g r^2}} - \frac{\frac{1}{2}\rho A C_d v^2}{m + I\frac{G_l^2}{n_g r^2}} \tag{5}$$

The time derivative of velocity is approximated using the finite difference method, where acceleration is calculated as the difference between two consecutive velocity values divided by the corresponding time step, thereby yielding the system of differential equations in discrete form:

$$v_{n+1} = v_n + \delta_t \left(\frac{n_t \frac{G_l}{r} T_{m,max} - mgf}{m + I\frac{G_l^2}{n_g r^2}} - \frac{\frac{1}{2}\rho A C_d v_n^2}{m + I\frac{G_l^2}{n_g r^2}} \right) \tag{6}$$

$$v_{n+1} = v_n + \delta_t \left(\frac{n_t \frac{P_E}{v_n}}{m + I\frac{G_l^2}{n_g r^2}} - \frac{mgf}{m + I\frac{G_l^2}{n_g r^2}} - \frac{\frac{1}{2}\rho A C_d v_n^2}{m + I\frac{G_l^2}{n_g r^2}} \right) \tag{7}$$

2.3. Dynamic model of the amphibious vehicle in underwater operation

When the amphibious vehicle operates in the water environment, system motion is sustained as long as the thrust T generated by the propeller is sufficient to overcome the total hydrodynamic resistance R_T acting on the vehicle hull. Due to the geometric similarity of the amphibious vehicle hull to a displacement-type ship hull, the total hydrodynamic resistance is determined using the semi-empirical Holtrop–Mennen method, which is widely applied in ship hydrodynamics analysis [24].

$$R_T = R_F(1 + k_1) + R_{APP} + R_W + R_B + R_{TR} + R_A \tag{8}$$

According to this formulation, the total resistance of the amphibious vehicle is the sum of the following components: frictional resistance with hull form factor $(R_F(1 + k_1))$, resistance of appendages (R_{APP}), wave-making resistance (R_W), additional pressure resistance of the bulbous bow near the waterline (R_B), additional pressure resistance of the immersed stern (R_{TR}), and model-ship correction resistance (R_A).

Since the hull design of the Amphibious Vehicle in this study does not include a bulbous bow or significant appendages, the two components R_{APP} and R_B are assumed to be zero. Accordingly, the total resistance is simplified as:

$$R_T = R_F(1 + k_1) + R_W + R_{TR} + R_A \tag{9}$$

$$R_T = \tfrac{1}{2}\rho C_F S_{BH} v^2 (1+k_1) + \rho g V_c c_1 c_2 c_5 \; exp\left\{m_1 F_n^d + m_4 cos(\lambda F_n^{-2})\right\} \\ +\tfrac{1}{2}\rho C_6 A_T v^2 + \tfrac{1}{2}\rho C_A S_{BH} v^2 \tag{10}$$

In the water operating mode, the motion of the amphibious vehicle is sustained by the thrust T generated by the electric motor and transmitted through the powertrain to the propeller. This thrust must be sufficient to balance and overcome the total hydrodynamic resistance acting on the vehicle hull. Accordingly, the longitudinal force equilibrium equation in the water environment is established as follows:

$$T = \tfrac{1}{2}\rho C_F S_{BH} v^2 (1+k_1) + \rho g V_c c_1 c_2 c_5 \; exp\left\{m_1 F_n^d + m_4 cos(\lambda F_n^{-2})\right\} \\ +\tfrac{1}{2}\rho C_6 A_T v^2 + \tfrac{1}{2}\rho C_A S_{BH} v^2 + ma + \tfrac{K_T}{K_Q} \cdot I \cdot \tfrac{G_w^2}{n_g D^2} \cdot a \tag{11}$$

where S_{BH} is the wetted surface area of the vehicle, which depends on shape coefficients and is determined by the following equation:

$$S_{BH} = L_{WL}(2T+B)\sqrt{C_M}\begin{pmatrix} 0.4530 + 0.4425C_B - 0.2862C_M \\ -\,0.003467\dfrac{B}{T} + 0.3696C_{WP} + 2.38\dfrac{A_{BT}}{C_B}\end{pmatrix} \tag{12}$$

The key geometric parameters of the amphibious vehicle hull include the block coefficient (C_B), the waterplane area coefficient (C_{wp}), and the midship section coefficient (C_M), which are determined based on the volume of the submerged portion of the hull. This set of geometric quantities, together with the Froude number (F_n) and Reynolds number (R_n), serves as the primary input parameters for the Holtrop–Mennen algorithm.

The block coefficient C_B is calculated using the following formula:

$$C_B = \frac{V_C}{L_{WL} \cdot B_{WL} \cdot T} \tag{13}$$

where V_C is the volume of the submerged hull, L_{WL} is the waterline length (m), B_{WL} is the waterline beam (m), and T is the draft of the vehicle (m). These quantities are determined through geometric analysis of the 3D design model (**Figure 3**). Specifically, the hull model is intersected by the waterplane corresponding to the static equilibrium condition according to Archimedes' principle. The volume of the hull below this plane is calculated using the volume analysis tool integrated in the CAD software, allowing for precise extraction of the submerged volume V_C. At the same time, characteristic geometric dimensions such as L_{WL}, B_{WL}, and T are directly obtained from the intersection contours between the hull and the waterplane.

The waterplane area coefficient C_{WP} depends on the waterline cross-sectional area A_{WP}:

$$C_{WP} = \frac{A_{WP}}{L_{WL} \cdot B_{WL}} \tag{14}$$

The area A_{WP} is determined by performing a cross-sectional cut of the 3D model at the design waterline, corresponding to the vehicle's static equilibrium according to Archimedes' principle. After identifying the waterplane at the floating equilibrium condition, the cross-sectional area is extracted using the geometric analysis function in the CAD software (**Figure 4**), ensuring high accuracy of the input parameter for the hydrodynamic model.

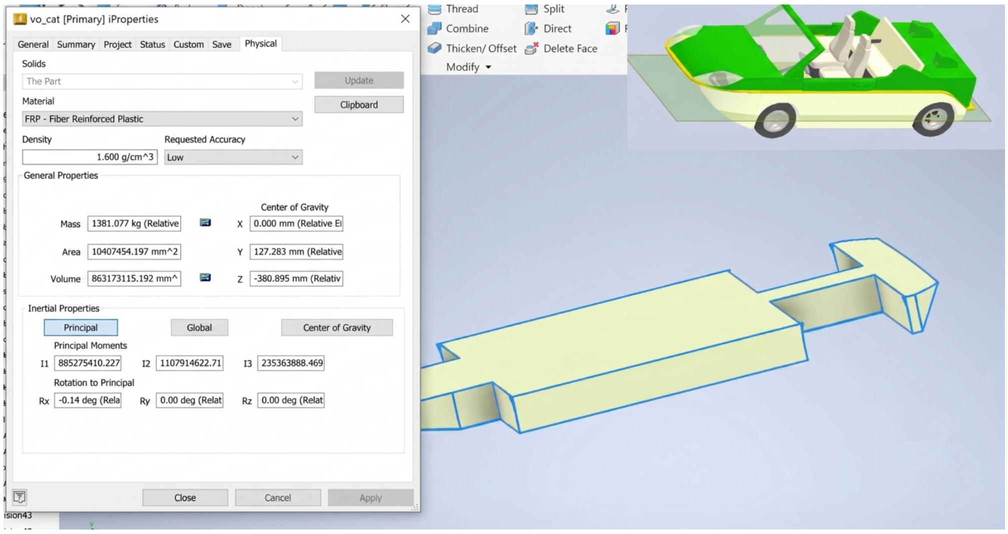

Figure 3. Submerged volume of the designed amphibious vehicle.

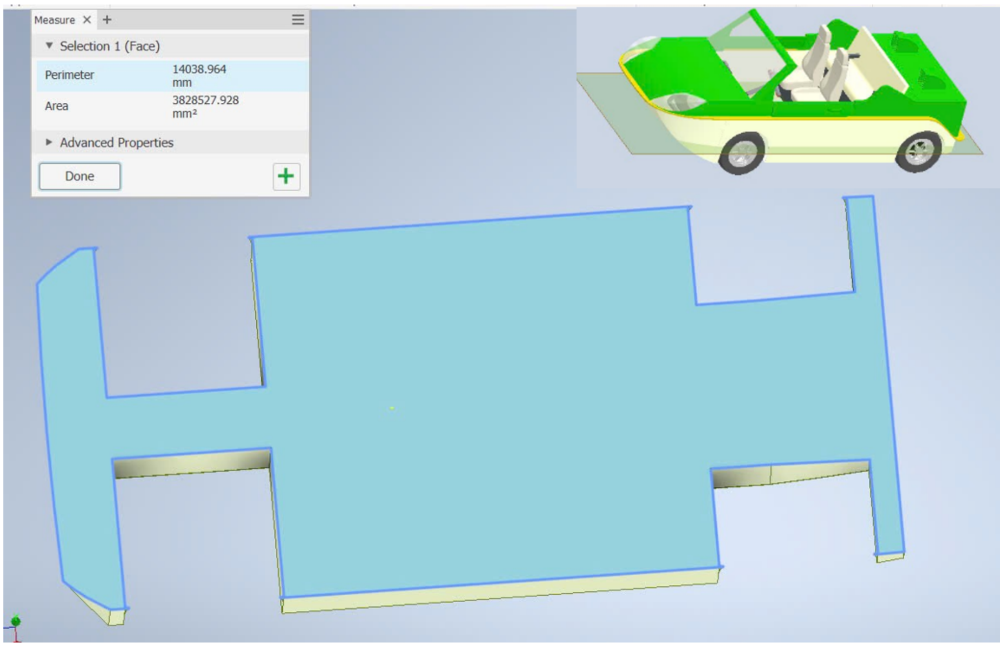

Figure 4. Waterline cross-sectional area of the designed vehicle.

The midship section coefficient C_M is influenced by the cross-sectional area of the submerged midsection of the Amphibious Vehicle hull A_M:

$$C_M = \frac{A_M}{B_{WL} \cdot T} \tag{15}$$

Similarly, the value of A_M is determined by performing a cross-sectional cut perpendicular to the vehicle's longitudinal axis at the midship section, corresponding to the plane at the midpoint of the waterline length (**Figure 5**).

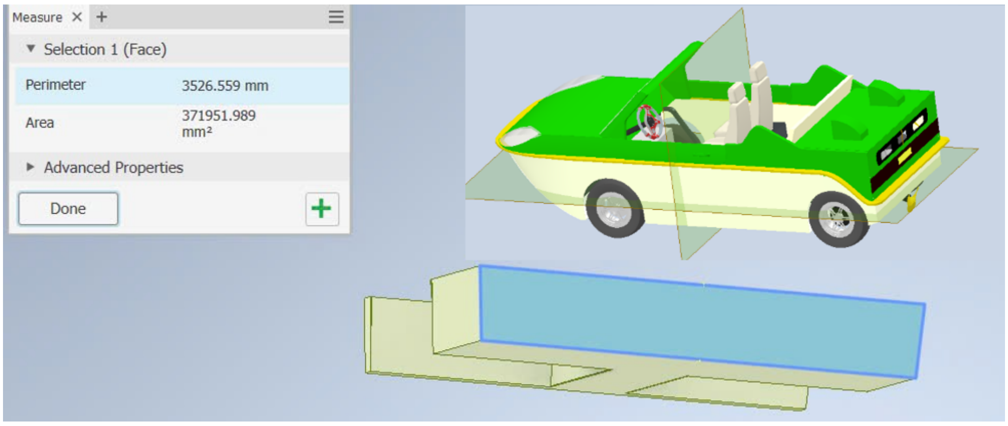

Figure 5. Cross-sectional area of the submerged midship of the designed amphibious vehicle.

The motor's moment of inertia is not specified. Therefore, an approximate calculation is applied by increasing the mass by 5% in Equation (11) and neglecting the term $\frac{K_T}{K_Q} \cdot I \cdot \frac{G_w^2}{n_g D^2} \cdot a$ to account for the effect of rotating masses.

Based on the overall powertrain layout of the Amphibious Vehicle proposed in this study (**Figure 1**), dimensionless quantities play an important role in analyzing the required thrust. Among them, the thrust coefficient K_T and the torque coefficient K_Q are two fundamental parameters that need to be considered [24].

Propeller thrust coefficient:

$$K_T = \frac{T}{\rho n^2 D^4} \tag{16}$$

Torque coefficient:

$$K_Q = \frac{Q}{\rho n^2 D^5} \tag{17}$$

where T(N) is the propeller thrust, Q is the propeller torque (N·m), ρ(kg/m^3) is the water density, n(rev/min) is the propeller rotational speed, and D(m) is the propeller diameter.

When the amphibious vehicle moves in the water environment, with a water density of 1,025 kg/m^3, the equation becomes:

$$\begin{aligned} \frac{K_T}{K_Q} \cdot \frac{G_w}{D} \cdot T_m &= \tfrac{1}{2}\rho C_F S_{BH} v^2 (1 + k_1) + R_W + \tfrac{1}{2}\rho C_6 A_T v^2 \\ &+ \tfrac{1}{2}\rho C_A S_{BH} v^2 + \left(m + \frac{K_T}{K_Q} \cdot I \cdot \frac{G_w^2}{n_g D^2}\right) a \end{aligned} \tag{18}$$

where T_m is the torque of the electric motor; G_w is the gear ratio of the powertrain connecting the electric motor to the propeller shaft (underwater section); and D is the propeller diameter.

In the initial stage, when the electric motor torque is constant, from Equation (14), it follows that:

$$\frac{dv}{dt} = \frac{n_g \cdot \frac{K_T}{K_Q} \cdot \frac{G_w}{D} \cdot T_{m,max}}{m + \frac{K_T}{K_Q} \cdot I \cdot \frac{G_w^2}{n_g D^2}} - \frac{\frac{1}{2}\rho C_F S_{BH} v^2 (1+k_1) + R_W + \frac{1}{2}\rho C_6 A_T v^2 + \frac{1}{2}\rho C_A S_{BH} v^2}{m + \frac{K_T}{K_Q} \cdot I \cdot \frac{G_w^2}{n_g D^2}} \tag{19}$$

This equation remains valid until the torque begins to decrease, at which point the power remains constant and the torque decreases hyperbolically as the electric motor speed increases. From Equation (14), the velocity is then governed by the following differential equation:

$$\frac{dv}{dt} = \frac{n_g \cdot \frac{K_T}{K_Q} \cdot \frac{P_E}{v}}{m + \frac{K_T}{K_Q} \cdot I \cdot \frac{G_w^2}{n_g D^2}} - \frac{\frac{1}{2}\rho C_F S_{BH} v^2 (1+k_1) + R_W + \frac{1}{2}\rho C_6 A_T v^2 + \frac{1}{2}\rho C_A S_{BH} v^2}{m + \frac{K_T}{K_Q} \cdot I \cdot \frac{G_w^2}{n_g D^2}} \tag{20}$$

In the numerical simulation process, the time derivative of the velocity v is approximated using the finite difference method in time. Specifically, the acceleration at a discrete time step is determined by the difference between two consecutive velocity values divided by the time step Δt. Consequently, the continuous differential equation of the system is rewritten as follows:

$$v_{n+1} = v_n + \delta_t \left(\begin{array}{c} \frac{n_g \cdot \frac{K_T}{K_Q} \cdot \frac{P_E}{v_n}}{m + \frac{K_T}{K_Q} \cdot I \cdot \frac{G_w^2}{n_g D^2}} \\ - \frac{\frac{1}{2}\rho C_F S_{BH} v_n^2 (1+k_1) + R_W + \frac{1}{2}\rho C_6 A_T v_n^2 + \frac{1}{2}\rho C_A S_{BH} v_n^2}{m + \frac{K_T}{K_Q} \cdot I \cdot \frac{G_w^2}{n_g D^2}} \end{array} \right) \tag{21}$$

2.4. Dynamic model of the amphibious vehicle during the transition from the underwater environment to dry land

Hydrodynamic resistance and tractive effort vary during three distinct periods during the HEPS transition from the aquatic to the terrestrial environment, according to analysis: (i) the fully submerged phase (**Figure 6a**), (ii) The wetted hull first makes contact with the ramp's terrestrial substrate through the front wheels during the ingress interface phase (**Figure 6b**), and (iii) the fully emerging climbing phase (**Figure 6c**). The accurate identification of bifurcation locations where the vehicle's dominating dynamic regimes change during the aquatic-to-terrestrial transition is made easier by this phased classification [20]

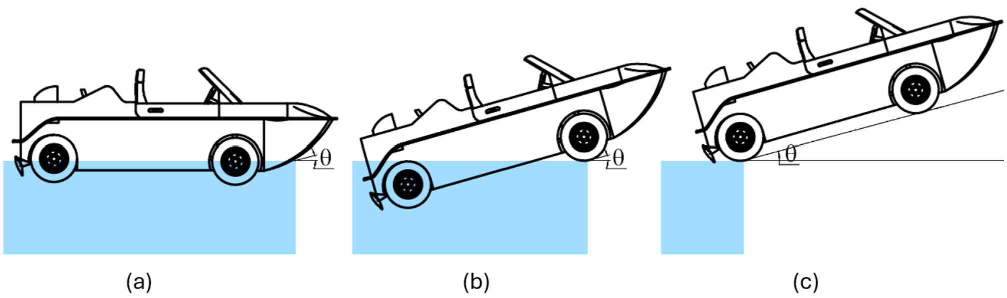

Figure 6. The transition of the HEPS from the underwater environment to dry land. **(a)** The amphibious vehicle has just reached the land-water boundary; **(b)** The amphibious vehicle's two front wheels have exited the water, while its two rear wheels remain submerged; **(c)** The amphibious vehicle has completely exited the water.

Based on the evolution of the contact interface morphology between the amphibious platform and the free surface across the three aforementioned phases. **Figure 7** illustrates an analytical geometric framework designed to quantitatively define the interdependencies among governing geometric parameters during the aquatic-to-terrestrial transition from the aquatic to the terrestrial environment.

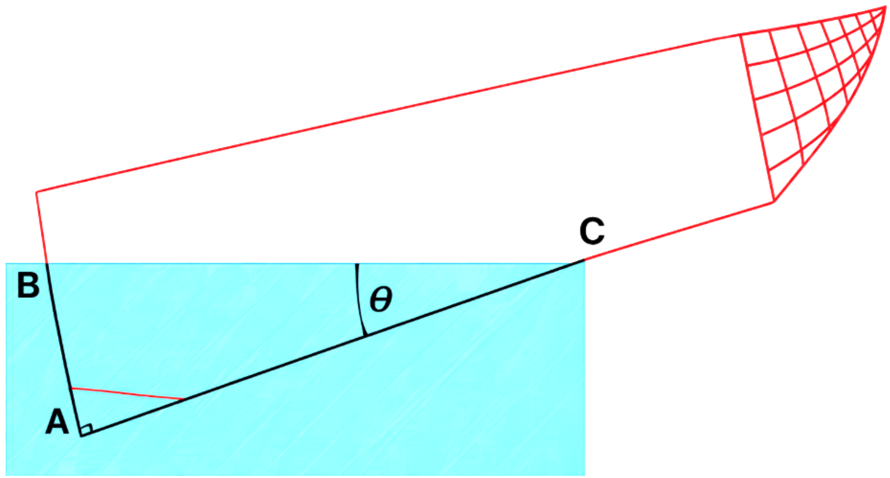

Figure 7. Relationship between the draft d (segment AB) and the waterline length L_{wl} (segment BC) as functions of the travel distance s (segment AC) of the amphibious vehicle.

In the transition phase, the draft d, waterline length L_{wl}, and waterline beam B_{wl} are treated as time-varying geometric parameters for updating buoyancy and hydrodynamic resistance. At the initial water-to-land transition condition (s = 0), the maximum draft is determined from the quasi-static hydrostatic equilibrium between the vehicle weight and the Archimedes buoyancy force. Using the block-coefficient approximation, the displaced volume can be expressed as $V_c = L_{wl,0} \cdot B_{wl,0} \cdot d_0 \cdot C_B$, and the equilibrium condition becomes $mg = \rho \cdot g \cdot L_{wl,0} \cdot B_{wl,0} \cdot d_0 \cdot C_B$. Therefore, the initial draft is obtained as $d_0 = \frac{m}{\rho \cdot L_{wl,0} \cdot B_{wl,0} \cdot C_B}$, where m is the vehicle mass, ρ is the water density, and $L_{wl,0}$, $B_{wl,0}$, and C_B are the initial waterline length, waterline beam, and block coefficient, respectively [21]. If heel is considered, the maximum draft can be corrected by adding the vertical draft increment induced at the lower side of the hull as follows [21]:

$$d_{max} = d_0 + \frac{B_{wl,0}}{2}\, tan\phi \tag{22}$$

where ϕ is the heel or trim angle. In the present longitudinal transition model, lateral heel and roll motions are neglected; therefore, $\phi = 0$ and $d_{max} = d_0$.

As the vehicle moves upward along the inclined slipway, the still-water surface is assumed to remain horizontal. For a longitudinal displacement s along a slipway with inclination angle θ, the vertical elevation of the vehicle relative to the water surface is sinθ. Hence, the instantaneous draft decreases according to $d(s) = d_{max} - s \cdot\ sin\theta$. To avoid a non-physical negative draft after full emergence, the draft is limited as $d(s) = max\,(0,\ d_{max} - s\ sin\theta)$. The theoretical full-emergence distance is then $s_{emerge} = \frac{d_{max}}{sin\theta}$; When $s \geq s_{emerge}$, the submerged draft becomes zero and the hull-related hydrodynamic resistance is no longer considered.

The instantaneous waterline length is updated from the geometric relationship between the remaining draft and the slipway inclination $L_{wl}(s) = \frac{d(s)}{tan\theta}$. For a vertical-side hull, B_{wl} can be treated as approximately constant. For a flared or trapezoidal hull cross-section, the waterline beam can be updated as $B_{wl}(s) = B_{wl,TK} + 2\,[d(s) - d_{TK}]\, tan\beta$, where $B_{wl,TK}$ is the design waterline beam, d_{TK} is the design draft, and β is the side-flare angle [21]. Consequently, $d(s)$, $L_{wl}(s)$, and $B_{wl}(s)$

provide the geometric inputs for continuously updating submerged volume, buoyancy, wetted surface area, and hydrodynamic resistance during the water-to-land transition.

To validate these relationships, this study adopts the Longitudinal Section Method, wherein the hull is modeled as a rigid geometric primitive within a Cartesian coordinate system. As the vehicle negotiates the incline, the free-surface intersection generates a time-variant sectional profile. Utilizing the geometric similarity assumption, the variables d, L_{wl}, and s are mapped onto the analytical triangle ABC, where the hypotenuse s represents the center of gravity (CG) trajectory. This trigonometric abstraction facilitates the normalization of complex kinematic variables into trigonometric functions, ensuring computational precision for shoreline-contact coordinates and establishing a robust framework for subsequent numerical simulations. The resultant force vectors acting on the vehicle during this transition are illustrated in **Figure 8**.

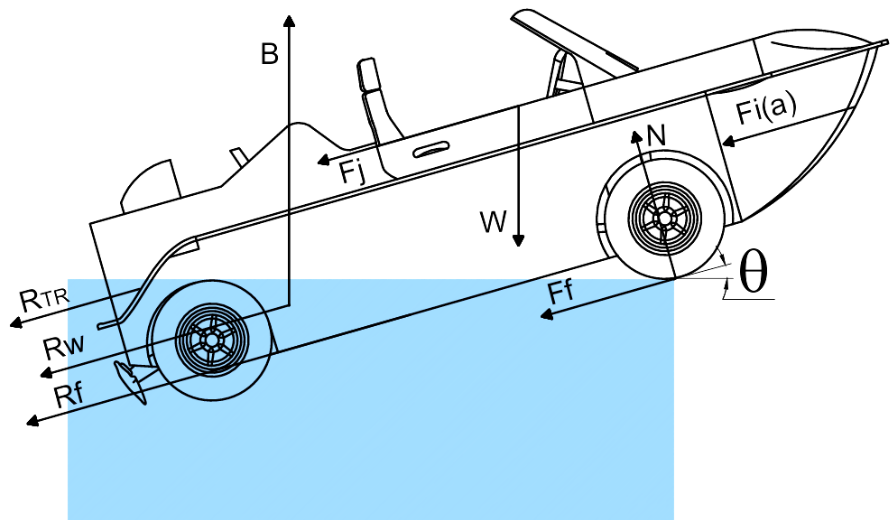

Figure 8. Analysis of the force distribution acting on the vehicle during the transition from the underwater environment to dry land.

Figure 8 illustrates the force distribution acting on the amphibious vehicle during the aquatic-to-terrestrial transition. At the investigated temporal instant, the vehicle exists in a dual-medium interaction state: the aft section (posterior to the front axle) remains submerged and is subjected to hydrodynamic resistance and hydrostatic buoyancy, whereas the fore section (anterior to the front axle) has fully emerged. Consequently, the front wheel assembly has established contact with the terrestrial substrate, initiating the tractive engagement phase [20].

Within the tire-ground interface on the terrestrial incline, the governing mechanical resistance components comprise the grade resistance (F_i), defining the static equilibrium threshold against longitudinal slip; the rolling resistance (F_f), stemming from hysteretic tire deformation and soil compaction; and the inertial resistance (F_j) associated with transient acceleration. To maintain model fidelity and prevent redundancy, the aerodynamic drag (F_ω) on the emerged superstructure is neglected, as it is subsumed within the total hydrodynamic resistance formulation [25].

Concurrently, the submerged hull volume is subjected to hydrodynamic resistance components formulated in accordance with ITTC (International Towing Tank Conference) standards, specifically: frictional resistance (R_f), which is a function of the time-variant wetted surface area; wave-making resistance (R_ω); transom pressure resistance (R_{TR}), arising from flow separation at the stern; and the correlation allowance (R_A). Additionally, the buoyancy force (B), acting through the center of buoyancy (CB), significantly influences the redistribution of normal ground reaction forces [24]. These interactions establish the analytical foundation for the equations of motion (EoM) governing the amphibious vehicle during the aquatic-to-terrestrial transition.

Derived from the tractive force equilibrium, the resistive load acting on the front axle during the partial-ingress phase is categorized into three primary components. First, the rolling resistance (F_f) exerted on the leading wheels is defined by: $F_f = 0.48 \cdot m \cdot g \cdot f \cdot cos\theta = 0.094176\, cos\theta(N)$, representing the hysteretic energy dissipation at the tire-substrate interface. Second, the grade resistance (F_i) is formulated by accounting for the countervailing buoyancy force (B) against the gravitational load (G): $F_j = (G - B)\ sin\theta = (G - \rho \cdot g \cdot V_c)\ sin\theta = 9.81m\ sin\theta - 11578.5088d^2$, this relationship demonstrates that the longitudinal grade resistance is a direct function of the instantaneous draft (d) of the submerged hull. Regarding aerodynamic drag (F_ω), since the front axle is non-ballasted/non-driven and does not contribute to tractive effort, the total air resistance is allocated to the driven rear axle. Consequently, to ensure mathematical consistency and prevent force redundancy, this component is excluded from the front-axle free-body analysis while the rear assembly remains submerged. Furthermore, although the front wheel assembly is non-driven, it must undergo angular acceleration proportional to the vehicle's translational acceleration. The rotational inertia of these components constitutes an additional resistive torque; consequently, the inertial resistance (F_j) is adjusted using a mass correction factor. Specifically, an empirical approximation is employed by increasing the effective vehicle mass by 5% (to account for rotating mass effects) while omitting the explicit polar moment of inertia term [23]. The total resistive load acting on the front axle is thus the vector sum of these components, formulated as:

$$F_{resistive\ force} = 0.48.m.g.f.cos20 + (G - \rho \times g \times V_c)\,sin20 + 1.05.m.a \tag{23}$$

The submerged resistance components are further defined in accordance with [23]:

$$\begin{gathered} R_T = R_F + R_\omega + R_{TR} + R_A = \\ \frac{1}{2}\rho C_F S_{BH} V^2 \{0.93 + 0.487118 \cdot C_{14} \left(\frac{B}{L_{WL}}\right)^{1.06806} \cdot \left(\frac{T}{L_{WL}}\right)^{0.46106} \cdot \left(\frac{L_{WL}}{L_R}\right)^{0.121563} \cdot \left(\frac{L_{WL}^3}{V_c}\right)^{0.36486} \cdot (1 - C_P)^{-0.60247}\} \\ + \rho g V_c C_1 C_2 C_5 \exp\left\{m_1 F_n^d + m_4\, cos\left(\lambda F_n^{-2}\right)\right\} + \frac{1}{2}\rho C_6 A_T V^2 + \frac{1}{2}\rho C_A S_{BH} V^2 \end{gathered} \tag{24}$$

In analyzing the egress phase of the amphibious vehicle, three hydrostatic parameters vary significantly as a function of the instantaneous draft (d): the displaced volume (V_c), the wetted surface area (S_{BH}), and the midship sectional area (A_T). The simultaneous attenuation of these quantities governs the reduction in hydrodynamic drag during the aquatic-to-terrestrial transition. Specifically, the wetted area (S_{BH})

defines the viscous interface between the hull and the fluid medium while the aft section remains submerged, directly influencing both frictional and wave-making resistance. As the vehicle ascends the incline, the draft (d) decreases relative to the displacement trajectory (s), causing S_{BH} to diminish near-linearly, which facilitates a rapid decay in hydrodynamic resistance. This parameter is calculated as follows [18]: $S_{BH} = L_{WL}(2d + B_{max}C_m)\sqrt{1 + \frac{1}{2}C_{WP}} = \frac{d(2d+1.5043)\sqrt{1.37}}{sin\theta}$. Concurrently, the displaced volume (V_c) dictates the buoyancy magnitude $(B = \rho \cdot g \cdot V_c)$, which modulates the hydrodynamic load components. As the draft (d) recedes, V_c decreases according to: $V_c = L_{WL}B_{max}dC_b = \frac{d}{sin\theta}BdC_b = \frac{1.18048d^2}{sin\theta}$, causing the buoyant support to diminish toward zero upon full emergence. This transition induces a significant redistribution of wheel loads and a subsequent shift in the vehicle's dynamic response. Additionally, the midship sectional area $A_T = C_mBd = 1.701d$ represents the maximum submerged transverse profile. Consequently, the total resistive load acting on the rear axle is formulated as the summation of wave-making resistance $R_W = \frac{267d^2}{sin\theta}$, transom pressure resistance $R_{TR} = 850.5dV^2$, viscous resistance $R_F = 1.4V^2\frac{d(2.34d+1.99)}{\sin\theta}\left(0.93 + 1.67354\frac{\sin^{0.7994}\theta}{d^{0.7032}}\right)$, and model–ship correlation allowance $R_A = 0,4V^2\frac{d(2,34d+1,99)}{sin\theta}$: $R_T = V^2\frac{d(2.34d+1.99)}{\sin\theta}\left(1.702 + 2.342956\frac{\sin^{0.7994}\theta}{d^{0.7032}}\right) + \frac{267d^2}{\sin\theta} + 850.5dV^2$.

By integrating these submerged drag vectors with the terrestrial tractive resistances generated upon front-wheel engagement, the governing equation of motion (EoM) for the HEPS during the aquatic-to-terrestrial transition on an inclined plane is established as follows:

$$\begin{gathered} F_{res} + R_T = 0.094\ \cos\theta + m\left(9.81\ \sin\theta + 1.05a\right) + \\ V^2d\left[850.5 + \frac{2.34d+1.99}{\sin\theta}\left(1.702 + 2.343\frac{\sin^{0.8}\theta}{d^{0.7}}\right)\right] + d^2\left(\frac{267}{\sin\theta} - 11,578.5\right) \end{gathered} \tag{25}$$

Based on longitudinal force equilibrium along the displacement vector on an inclined plane of angle θ, the system is modeled as an equivalent mass (m) subjected to the total submerged resistance $R_\omega(d, V)$, the terrestrial resistive load F_{res}, and the resultant gravitational-buoyancy vector acting along the slope. Both the hydrostatic buoyancy and the hydrodynamic drag are functions of the instantaneous draft (d) and translational velocity (V). By applying Newton's Second Law to the rectilinear motion of the HEPS along the inclined substrate, the governing differential equation for the vehicle's longitudinal acceleration is derived as follows [26]:

$$\dot{u} = \frac{1}{m}\left(T_j - F_{res} - R(V, d, \theta)\right) + vr \tag{26}$$

2.5. Model assumptions and limitations

The proposed dynamic framework was developed under simplified operating conditions to ensure computational efficiency and focus on the dominant propulsion behavior of the amphibious vehicle. Calm-water conditions and purely longitudinal motion were assumed, while disturbances such as waves, water currents, crosswinds, suspension dynamics, lateral–yaw coupling, and deformable tire–soil interaction were neglected. Although these assumptions limit the representation of real-world operating conditions, they enable the development of a unified system-level framework suitable for preliminary propulsion analysis and trans-media dynamic evaluation. The modular force-balance structure also allows future integration of higher-fidelity hydrodynamic and terrain-interaction models. To justify the simplified assumptions adopted by Huang et al. [18], a quantitative error-boundary analysis was conducted for the neglected suspension compliance, tire–soil deformation, and wave/current disturbances. These effects are not ignored arbitrarily, but are evaluated to confirm their limited influence on the longitudinal traction prediction within the scope of paved slipway and calm-water operation.

First, the rigid-body assumption neglects the pitch motion induced by longitudinal load transfer during acceleration and climbing. The pitch angle can be estimated from the relationship $\theta_p = \frac{m.a_x.h_{CG}}{K_p}$, where m is the vehicle mass, a_x is the longitudinal acceleration, h_{CG} is the center-of-gravity height, and K_p is the equivalent suspension pitch stiffness [21]. In the present simulation, the maximum acceleration is approximately $a_x = 2.1$ m/s^2. Since the suspension stiffness is not explicitly modeled, a conservative upper-bound pitch angle of $\theta_p = 0.015$ rad (0.86°) is adopted. The resulting relative error in grade resistance is estimated as:

$$\varepsilon_{sup} = \left| \frac{sin(\alpha + \theta_p) - sin(\alpha)}{sin(\alpha)} \right| = \left| \frac{sin(20^\circ + 0.015) - sin(20^\circ)}{sin(20^\circ)} \right| \approx 4.1\% \quad (27)$$

where α is the slipway angle. For the maximum slipway angle of $\alpha = 20°$, the estimated error is below the 5% engineering threshold. Since grade resistance is only one component of the total resistance, the overall influence of neglected suspension pitch dynamics on the required traction force is expected to be smaller than this upper-bound value.

Second, the model assumes a rigid paved interface and does not explicitly include tire–soil deformation. For deformable terrain, the additional compaction resistance may be estimated using a Bekker-type relationship, $R_c = \frac{bk_{eq}z^{n+1}}{n+1}$, where b is the tire contact width, z is the tire sinkage, n is the soil deformation exponent, and k_{eq} is the equivalent pressure–sinkage modulus [19,20]. Under the paved slipway conditions considered in this study, tire sinkage approaches zero ($z \rightarrow 0$), and therefore the compaction resistance also approaches zero ($R_c \rightarrow 0$). The remaining tire-related effect is represented by the rolling resistance coefficient f_r, which has already been included in the longitudinal force-balance model. Thus, neglecting tire–soil deformation is consistent with the intended operating condition of concrete or asphalt transition surfaces.

Third, wave and current disturbances are neglected by assuming calm-water operation. For small-amplitude waves, the additional wave resistance is generally proportional to the square of the wave amplitude $\Delta R_{a\omega} \propto \xi_a^2$, where ξ_a is the wave amplitude. In the present simulation, the peak hydrodynamic resistance during transition is approximately R_{max} = 1,745.20 N. If the wave-induced disturbance is bounded within 3.5% of this peak value, the additional resistance is $\Delta R_{a\omega} < 0.035 R_{max} = 0.035 \times 1,745.20 \approx 61.1$ N. This value is small compared with the dominant mechanical and hydrodynamic resistance components in the baseline model. Therefore, the calm-water assumption is acceptable for preliminary longitudinal dynamic evaluation under calm or near-calm water conditions.

Overall, the quantitative estimates show that the neglected suspension effect remains below approximately 4.1%, tire–soil compaction resistance approaches zero on paved slipways, and small wave-induced resistance is limited to about 61.1 N. These results support the validity of the simplified longitudinal model for preliminary Series HEPS propulsion sizing. Nevertheless, the model is mainly applicable to paved-interface and calm-water conditions; future work should include suspension dynamics, Bekker-based terramechanics, wave spectra, and current-induced hydrodynamic excitation for more severe operating environments.

In addition to the neglected dynamic effects discussed above, the linear geometric transition assumption was also evaluated through a CAD-based volumetric sensitivity analysis. In Section 2.4, the instantaneous draft $d(s)$ is modeled as a linear function of the longitudinal displacement s to enable continuous updating of buoyancy, wheel-load redistribution, and hydrodynamic resistance during the water-to-land transition [18,20]. Although real hull geometries may produce nonlinear variations in waterline shape and submerged volume due to bow curvature, stern geometry, and local cross-sectional changes, the amphibious vehicle considered in this study has a monolithic floating body with a relatively flat bottom, rounded bow, and slightly tapered stern. This geometry limits the nonlinear deviation from the linear draft attenuation model.

To quantify the influence of this simplification, the analytical submerged volume $V_{linear}(s)$ was compared with the CAD-extracted submerged volume $V_{CAD}(s)$ at different immersion depths. The volumetric error is defined as: $\varepsilon_{vol} = \left|\frac{V_{CAD}(s)-V_{linear}(s)}{V_{CAD}(s)}\right|$, where $V_{CAD}(s)$ is obtained from the CAD-based waterplane intersection method, while V_{linear}(s) is estimated from the linear draft attenuation model. The results show that the maximum deviation occurs during the initial emergence stage, where the rounded bow affects the waterline intersection. However, for the flat-bottom hull considered in this study, the maximum volumetric error remains below the 5% engineering threshold, with $\varepsilon_{vol,max} \leq 4.8\%$. Since the buoyancy force is directly proportional to the displaced volume, according to $B(s) = \rho g V(s)$, the corresponding buoyancy-force error is of the same order as the volumetric error. Therefore, the influence of the linear geometric transition assumption on buoyancy estimation and wheel-load redistribution is limited, confirming its suitability for preliminary longitudinal dynamic profiling and Series HEPS propulsion sizing during the water-to-land transition.

3. Results and discussion

3.1. Dynamic of the amphibious vehicle in the on-road phase

Figure 9 presents the simulated acceleration characteristics of the amphibious vehicle on a dry paved surface starting from a standstill, with load levels of 25%, 50%, 75%, and 100% of the design load. The results indicate that the vehicle mass directly affects both the time required to reach the speed limit of 60 km/h and the corresponding acceleration distance. At full load (860 kg), the vehicle reaches 60 km/h after approximately 28 s, with an acceleration distance of about 350 m. When the load is reduced to 75% (795 kg), 50% (730 kg), and 25% (665 kg), the times to reach 60 km/h decrease to approximately 25 s, 22 s, and 20 s, respectively, while the acceleration distance gradually increases to nearly 400 m. This trend is consistent with Newton's second law: under the same torque and power conditions, acceleration increases as mass decreases.

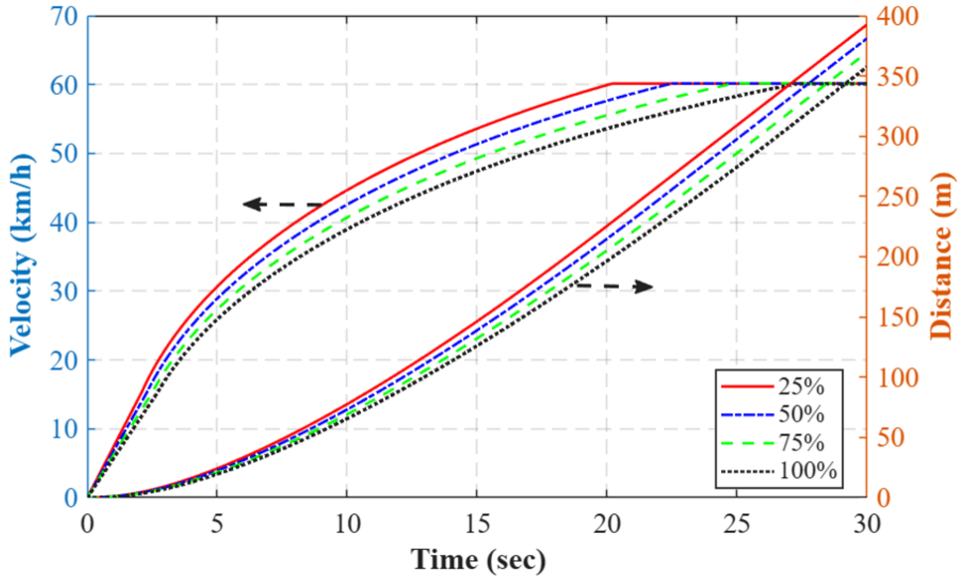

Figure 9. Velocity and travel distance of the amphibious vehicle under varying loads—On-road phase.

In the initial stage, the vehicle reaches 15 km/h after 2.8 s (100% load), 2.5 s (75%), 2.0 s (50%), and 1.8 s (25%). This corresponds to the electric motor's maximum torque region, where the traction force fully governs the motion because aerodynamic resistance is still small. Beyond the maximum torque region, the motor operates in the nearly constant power region; torque decreases with increasing rotational speed while aerodynamic drag rises with the square of velocity, causing acceleration to gradually diminish as speed increases. The velocity–time curve clearly illustrates the two characteristic regions of electric propulsion: the constant torque region and the constant power region.

The simulation results demonstrate that the extended-range hybrid propulsion system meets the acceleration requirements across the entire operational load range. At the same time, the agreement between the simulated characteristics and the fundamental dynamics of electric propulsion confirms the consistency and reliability of the developed vehicle dynamics model.

Figure 10 illustrates the variation of vehicle acceleration over time under different load conditions. Immediately after start-up, acceleration reaches its peak, approximately 1.52 m/s^2 at full load, increasing to about 2.1 m/s^2 when the load is reduced to 25%, reflecting the direct influence of inertial mass on acceleration capability. During the initial 0.3–3 s, acceleration remains nearly constant, corresponding to the electric motor's maximum torque region, where traction force dominates and aerodynamic drag is still small. Subsequently, as the motor enters the nearly constant power region, torque decreases with rotational speed while aerodynamic resistance rises with the square of velocity, resulting in a nonlinear decay of acceleration over time. Acceleration approaches zero as the speed reaches 60 km/h, where the traction force balances the total resistance, confirming stable operation and the design speed limit. This behavior clearly illustrates the two characteristic regions of electric propulsion and validates the consistency of the developed vehicle dynamics model.

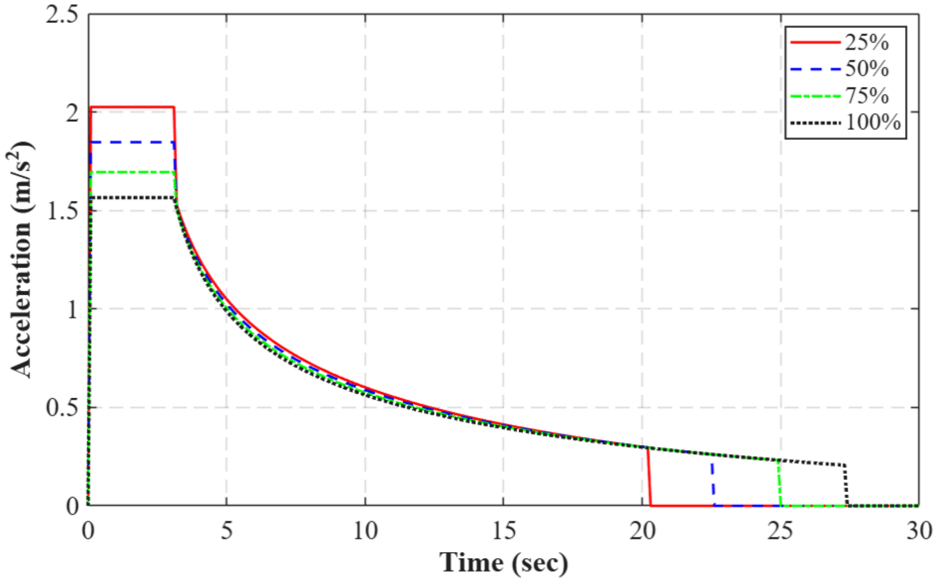

Figure 10. Variation of amphibious vehicle acceleration over time at different load levels.

Figure 11 illustrates the characteristic relationship between gradeability and speed of the amphibious vehicle at different load levels. The results indicate that as speed increases, the maximum maintainable slope decreases significantly. This trend reflects the power balance limitation of the propulsion system: at higher speeds, the power required to overcome the total resistance (particularly the slope resistance and aerodynamic drag) rises rapidly, while the available power from the powertrain remains limited.

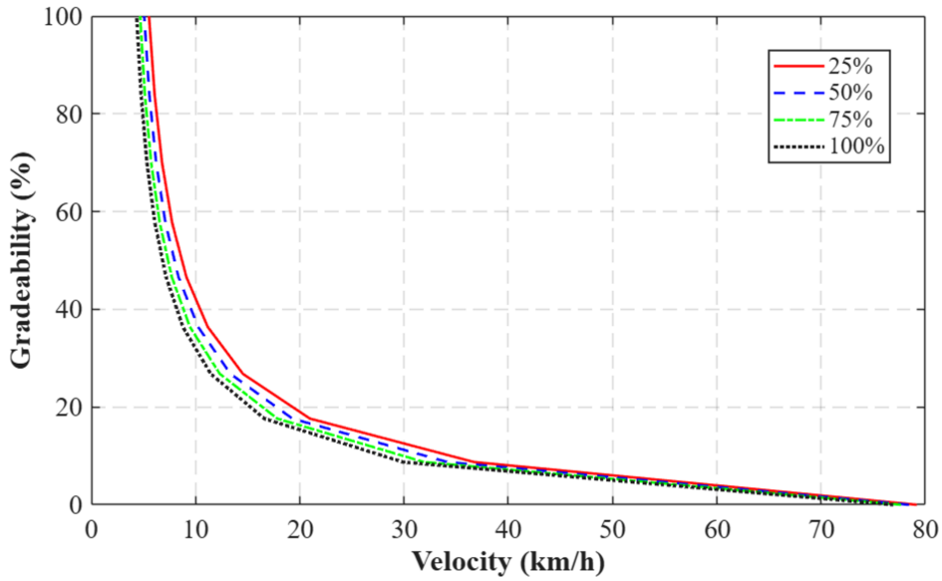

Figure 11. Simulation results of amphibious vehicle climbing ability under varying load—On land.

On level ground, the maximum speed reaches approximately 65 km/h. As the slope increases beyond 10% (≈5.7°), the maximum speed decreases to around 30 km/h. The reduction continues when the slope reaches 30–40% (≈16.7°–21.8°), where the maintainable speed drops to about 10 km/h depending on the load level. At a slope of approximately 100% (≈45°), the maximum speed decreases further to around 4.2–6.2 km/h. The spacing between the curves indicates the direct influence of vehicle load: the higher the load, the lower the gradeability at the same speed, since slope resistance is proportional to the total vehicle weight.

Mechanically, the slope resistance increases with the component of gravitational force along the incline, raising the torque demand at the wheels. Meanwhile, the characteristics of electric drive systems including the torque-limited region and the power-limited region cause a reduction in the ability to maintain high speeds on steep slopes. The convergence of the curves at higher speeds indicates that, as velocity increases, aerodynamic drag and power limitations become the dominant factors, relatively diminishing the influence of vehicle load compared to low speed conditions.

It should be clarified that the 100% gradeability case (≈45°) shown in **Figure 11** is only an idealized dry-road assessment of the maximum torque capability of the electric powertrain. This case is used to examine the propulsion margin for preliminary sizing and should not be interpreted as a feasible water-exit condition during aquatic-to-terrestrial transition. In the actual transition analysis, the vehicle is evaluated for bank slopes up to 20° (≈36.4%), which represents the maximum practical slipway angle considered in this study [18].

The present model is limited to longitudinal dynamics on paved or smooth slipway surfaces; therefore, lateral motion, yaw response, suspension dynamics, and deformable tire–soil interaction [19] are not included. Accordingly, the results should be interpreted as longitudinal propulsion feasibility rather than full six-degree-of-freedom stability prediction [20].

3.2. Amphibious vehicle dynamics—Underwater operation

Figure 12 shows the acceleration characteristics of the amphibious vehicle starting from rest in a still-water environment, with load levels ranging from 25% to 100% of the design load. The results indicate that the maximum speed underwater reaches approximately 8.7 km/h in all cases, reflecting the equilibrium limit between the propeller thrust and the total hydrodynamic resistance at steady state.

Under full load conditions (860 kg), the vehicle reaches its maximum speed after approximately 11 s, with an acceleration distance of about 43 m. When the load decreases to 75%, 50%, and 25%, the time to reach the limit speed shortens to around 8 s, 7 s, and 6 s, respectively, while the acceleration distance varies between 40–42 m. This trend indicates that the vehicle mass significantly affects the initial acceleration but has little impact on the final steady state speed, as the maximum speed is primarily governed by the propeller thrust characteristics and hydrodynamic resistance, which depend more strongly on velocity than on mass.

In the initial phase (0–3 s), the vehicle accelerates rapidly, reaching approximately 6 km/h within 2–3 s depending on the load. This corresponds to the operating region where the electric motor provides high torque and the propeller generates strong thrust, while wave resistance and frictional resistance remain relatively small. As the speed increases, hydrodynamic resistance rises nonlinearly with velocity, causing the acceleration to gradually decrease until the vehicle reaches a dynamic equilibrium, where the thrust equals the total resistance and the acceleration approaches zero.

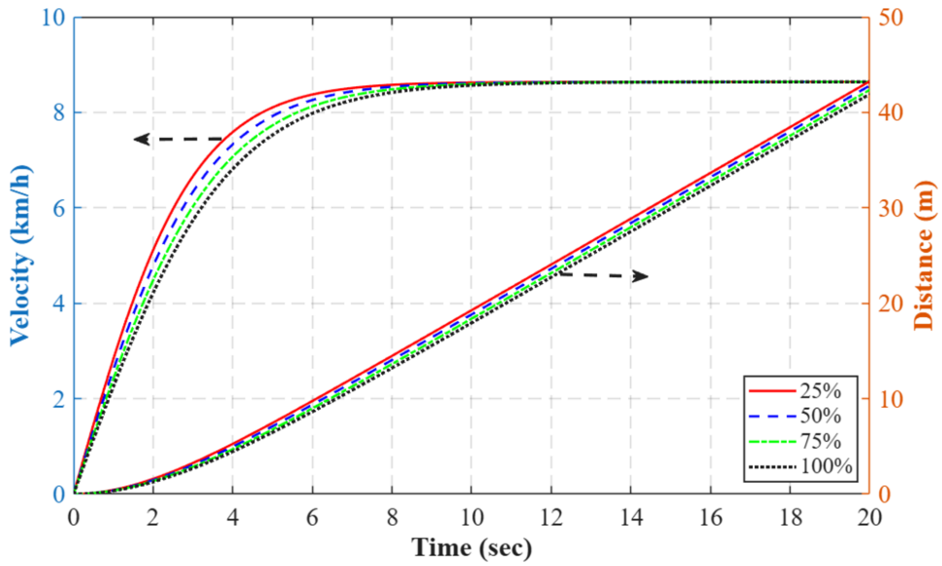

Figure 12. Velocity and distance of the amphibious vehicle as the load changes—On water.

The simulation results indicate that the limiting speed of approximately 9 km/h aligns well with the selected propeller configuration and power rating of the propulsion system. This value satisfies the requirements for safe and stable operation in a calm water environment, while also confirming the validity of the model representing the interaction between the electric drive system and the hydrodynamic characteristics of the vehicle hull.

3.3. HEPS dynamics during the transition from the underwater environment to dry land

3.3.1. Geometric relationships

The simulation results depicted in **Figure 13** demonstrate a robust correlation between the draft (d) and longitudinal displacement (s) during the littoral transition. The trajectories indicate that the effective draft undergoes a linear attenuation as the vehicle negotiates the slipway incline. This monotonic decreasing trend aligns with the computational framework of the present study, which assumes calm-water conditions to isolate the influence of fundamental geometric parameters from stochastic wave-induced perturbations.

Regarding payload sensitivity, the data indicate a substantial increase in the peak draft (d_{max}) as the vehicle mass scales from 665 kg (25% payload) to 860 kg (100% payload). Specifically, under nominal load conditions (100%), the draft reaches a maximum of 0.685 m at a longitudinal trim angle of θ = 20°. This increased payload shifts the initial hydrostatic equilibrium and expands the submerged projected area, thereby increasing the resistive torque demand on the powertrain during the initial ingress phase.

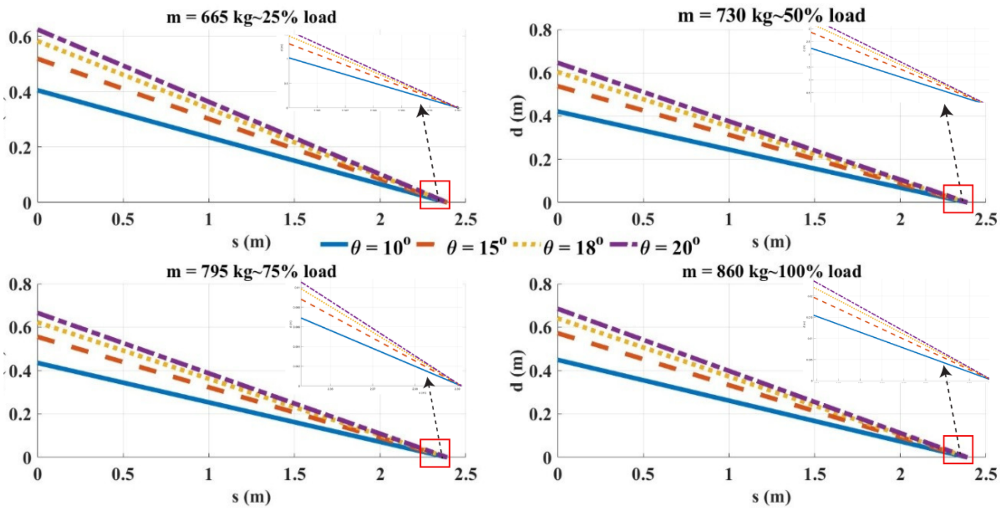

Figure 13. Correlation between instantaneous draft (d) and displacement trajectory (s).

Simultaneously, the trim angle (θ) serves as a governing kinematic variable modulating the rate of draft reduction $\left(\frac{\partial d}{\partial s}\right)$. As θ increases from 10° to 20°, the gradient of the d–s characteristic curves steepens, reflecting an accelerated transition in the submerged hull geometry. Consequently, the variance in d provides critical data for identifying the bifurcation point between buoyancy-dominated support and tractive-effort-dominated propulsion. These findings facilitate the optimization of intelligent power-distribution algorithms for amphibious operations in slipways and coastal landing zones.

3.3.2. Straight-line motion dynamics

Numerical results for the aquatic-to-terrestrial transition (**Figure 14**), initiated at a translational velocity of u = 0.5 m/s at s = 0 m, indicate that the longitudinal velocity (u(s)) undergoes non-linear acceleration across all payload configurations (m = 665–860 kg) and incline gradients (θ = 10°–20°). This kinematic behavior aligns with the longitudinal governing equations for calm-water conditions, where lateral degrees of freedom (DoF) are neglected. The terminal velocity at the conclusion of the transition phase (s = 2.391 m) is summarized in **Table 2**.

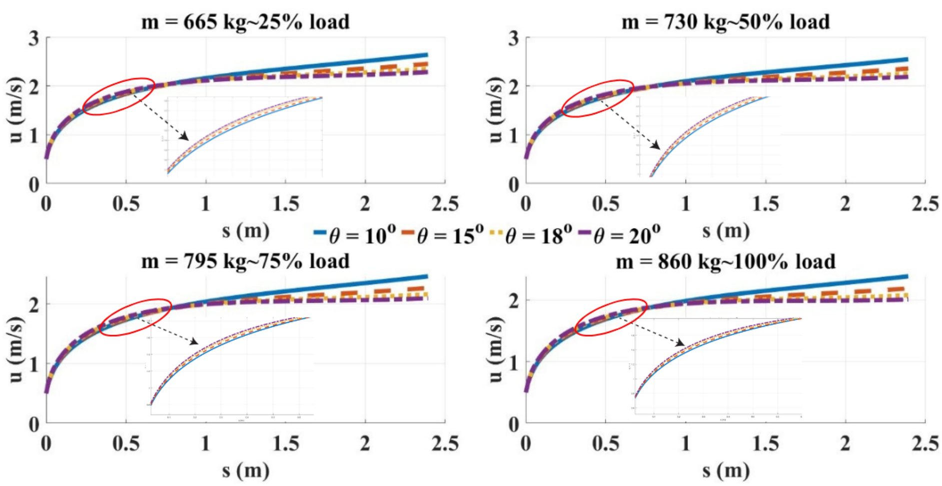

Figure 14. Variation of the velocity components u with respect to the travel distance.

Table 2. Terminal longitudinal velocity (m/s) at the transition boundary (s = 2.391 m) as a function of vehicle mass (m) and incline gradient (θ).

Vehicle mass m (kg)	θ = 10°	θ = 15°	θ = 18°	θ = 20°
665	2.64	2.45	2.35	2.28
730	2.55	2.36	2.25	2.19
795	2.46	2.27	2.16	2.09
860	2.38	2.19	2.08	2.01

The results indicate that longitudinal velocity u(s) is inversely proportional to both the vehicle mass (m) and the incline gradient (θ). Elevated values for these parameters exacerbate grade and inertial resistance, thereby attenuating net acceleration. The non-linear growth trajectory of u(s) corresponds to the exponential decay in hydrodynamic drag as the displaced volume recedes. Upon full emergence, the dynamic regime is governed primarily by rolling and grade resistance, aligning with standard terrestrial vehicle dynamics.

A significant phenomenon is observed during the initial transition phase ($0 \leq 0.4$ m), where u(s) at θ = 20° temporarily exceeds the velocity at θ = 10°. This velocity crossover indicates a shift in dominance between hydrodynamic drag and gravitational resistance. On steeper gradients, the submerged hull geometry contracts abruptly; consequently, the hydrodynamic resistance components vanish at a rate exceeding the simultaneous increase in grade resistance, yielding a localized acceleration surge. As the vehicle advances into the terrestrial phase, grade resistance emerges as the primary limiting factor, restoring the conventional inverse relationship between slope angle and velocity.

3.3.3. Resistance force

Numerical results for the combined mechanical resistance (F_c)—encompassing rolling resistance, buoyancy-corrected grade resistance, and inertial resistance—alongside the hydrodynamic drag (R) as functions of displacement (s) (**Figure 15**), delineate three discrete dynamic regimes. At the initial boundary (s = 0 m), F_c achieves its peak magnitude (**Table 3**) before undergoing rapid attenuation. The data indicate that initial F_c is inversely proportional to both the incline gradient (θ) and vehicle mass (m). This apparent paradox is elucidated by the quasi-static force balance; in the incipient phase, the volumetric displacement generates substantial hydrostatic buoyancy, which significantly mitigates the normal reaction force at the tire-substrate interface. Consequently, both the rolling resistance (F_f) and the longitudinal grade component are suppressed, an effect that supersedes the increase in inertial resistance associated with the initial acceleration phase.

A prominent dynamic phenomenon occurs in the intermediate region (s = 0.3–0.8 m), where F_c reaches a local minimum while the hydrodynamic drag (R) increases progressively to its peak magnitude. This inverse correlation stems from a shift in force dominance during the transition. As the vehicle accelerates, the longitudinal velocity (u(s)) increases, causing R to rise quadratically relative to velocity (**Table 4**) while a significant portion of the hull remains submerged. This elevated hydrodynamic resistance suppresses instantaneous acceleration, leading to a marked reduction in the inertial resistance component (F_j). Simultaneously, the residual buoyancy remains sufficient to maintain a low normal wheel load, preventing a significant rise in the baseline mechanical resistance. The synergy of suppressed acceleration and mitigated normal loads drives F_c to its minimum.

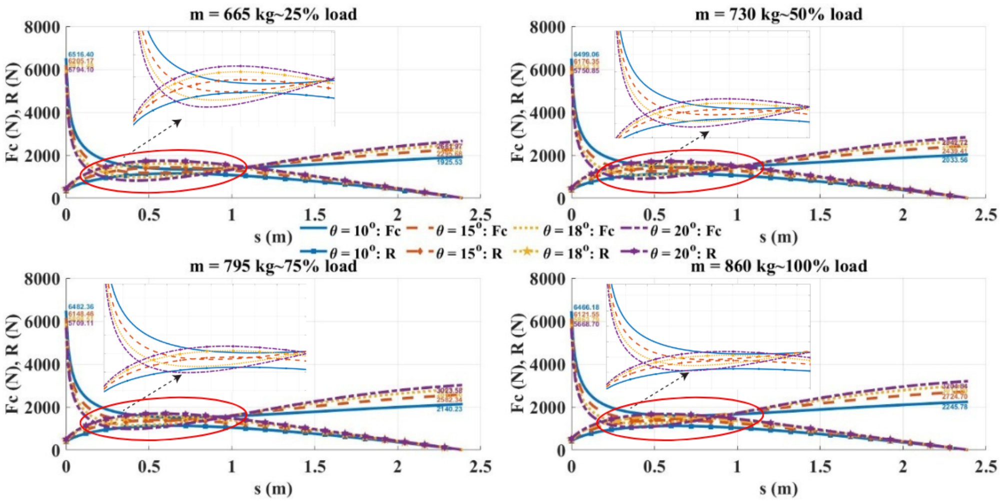

Figure 15. Variation of the total resistance force.

Table 3. Maximum mechanical resistance F_c(N) at s = 0 m

Vehicle mass m (kg)	θ = 10°	θ = 15°	θ = 18°	θ = 20°
665	6,516.40	6,205.17	5,971.48	5,794.10
730	6,499.06	6,176.35	5,934.33	5,750.85
795	6,482.36	6,148.46	5,898.51	5,709.11
860	6,466.18	6,121.55	5,863.79	5,668.70

Table 4. Mechanical resistance F_c(s) (N) at the end of the process, at s = 2.391 m.

Vehicle mass m (kg)	θ = 10°	θ = 15°	θ = 18°	θ = 20°
665	1,925.53	2,295.68	2,516.87	2,661.97
730	2,033.56	2,439.41	2,681.86	2,842.72
795	2,140.23	2,582.34	2,847.36	3,013.58
860	2,245.78	2,724.70	3,012.80	3,204.84

Upon traversing this crossover region, the hull undergoes progressive emergence, and the reduction in wetted surface area causes R to decay toward zero. Conversely, the attenuation of hydrostatic buoyancy transfers the total gravitational load to the suspension and wheel assemblies. The force equilibrium thus shifts entirely to terrestrial vehicle dynamics on an inclined plane, causing Fc to rebound. In this final phase, the resistance follows the expected fundamental trend: direct proportionality to both m and θ (**Table 4**).

In contrast to the monotonic attenuation of mechanical resistance during the initial stage, the purely hydrodynamic resistance (R(s)) does not peak at the transition origin (s = 0 m), but instead reaches its maximum magnitude within the intermediate transition zone (s = 0.4–0.6 m), as summarized in **Table 5**.

The data indicate that R_{max} is directly proportional to the incline gradient (θ) but inversely proportional to the vehicle mass (m). This payload-dependent reduction in R(s) stems from a coupled dynamic interaction: higher mass suppresses longitudinal acceleration, resulting in a lower instantaneous velocity (u(s)) within the intermediate region. Given that R scales quadratically with velocity (u^2), the reduction in this kinematic component overrides the influence of increased volumetric displacement, which would otherwise augment the drag.

Table 5. Maximum hydrodynamic resistance R(s) (N) in the intermediate transition region.

Vehicle mass m (kg)	θ = 10°	θ = 15°	θ = 18°	θ = 20°
665	1,151.60	1,436.60	1,616.76	1,745.20
730	1,138.95	1,417.49	1,593.65	1,719.17
795	1,128.50	1,401.27	1,573.64	1,696.50
860	1,119.92	1,387.37	1,556.38	1,676.83

The occurrence of a localized peak in R(s) at mid-slope is a consequence of competing dynamic and hydrodynamic effects. At s = 0 m, despite the maximum draft, the low velocity prevents R from reaching its peak. As the vehicle enters the intermediate region, u increases significantly while the wetted surface area remains substantial, yielding the peak hydrodynamic load. In the final phase, although velocity continues to rise, the rapid decay of the draft toward d = 0 causes the hull to fully emerge, leading to the evanescence of R(s).

In summary, the resistance characteristic curves facilitate the classification of the transition into three discrete dynamic phases: (i) the Incipient Phase, governed by hydro-terrestrial coupling where buoyancy mitigates normal tire loads and inertial effects dominate; (ii) the Intermediate Transition Phase, characterized by the simultaneous maximization of velocity and wetted area, causing a hydrodynamic surge that suppresses acceleration and drives the aggregate mechanical resistance to a local minimum; and (iii) the Terminal Phase, where hydrodynamic drag is eliminated, and the system reverts to conventional terrestrial vehicle dynamics on an inclined substrate.

3.3.4. Required power

The graph in **Figure 16** illustrates the evolution of the vehicle's power state (P) as a function of longitudinal displacement (s), elucidating the energy demand during the environmental transition phase. The simulation results depict the variation of the required power, P(s), with respect to distance under four load conditions and four bank slope angles. Consequently, the power curve reflects the synergistic effects of the submergence geometry d(s), the kinematic state u(s), and the distribution of longitudinal force components. A common characteristic across all scenarios is that P(s) does not originate from zero; rather, it increases sharply at the onset, reaches a peak in the intermediate region (s = 1.4–1.8 m), and subsequently decreases slightly towards the end of the stroke (s = 2.391 m), forming a distinct dome-shaped profile. At the initial position (s = 0 m), although the mechanical resistance component (F_c) is at its maximum, the required power fluctuates only within a moderate range of 3.4 to 3.6 kW, depending on the slope angle θ. This phenomenon stems from the boundary conditions of the problem: the vehicle enters the transition zone with an initial velocity of u = 0.5 m/s rather than starting from a standstill. In this very early stage (s = 0 to 0.3 m), a notable observation is that the required power at θ = 10° is actually higher than that at θ = 20°. This discrepancy can be explained by the specific trans-media dynamics: at a

20° angle, the reduction in draft occurs more rapidly in accordance with the geometric relationship, leading to an earlier decline in both buoyancy and hydrodynamic effects. More importantly, the vertical velocity u(s) at 10° during this phase is greater than at 20°. Since power is proportional to velocity, the difference in u(s) outweighs the difference in drag, resulting in Preq(s) at 10° being temporarily greater than at 20°. This is a characteristic phenomenon of the aquatic-terrestrial interaction phase, where velocity and buoyancy still exert a strong influence and are not yet completely overshadowed by mechanical grade resistance.

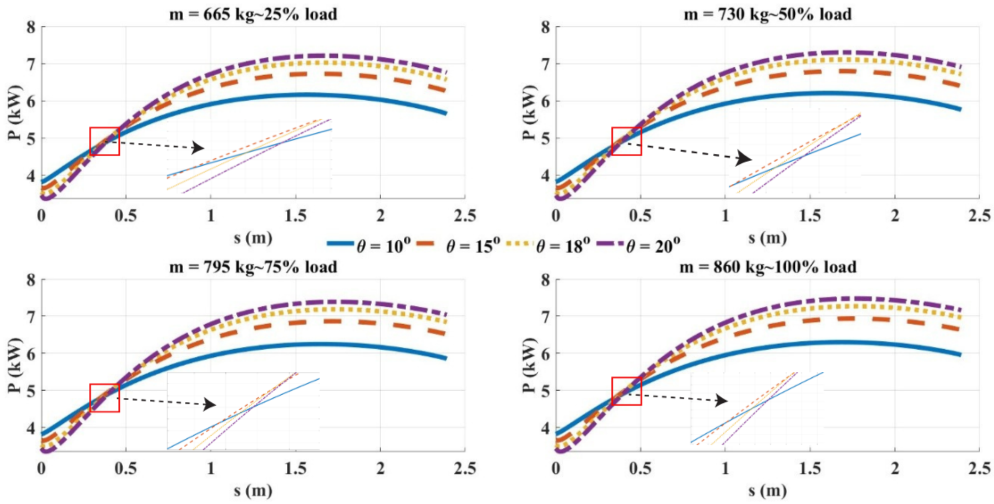

Figure 16. Variation of required power.

The variation in required power ($P_{req}(s)$) reflects the coupled influence of the submerged geometry (d(s)), the kinematic state (u(s)), and the distribution of longitudinal resistive loads. Across all simulated scenarios, the $P_{req}(s)$ trajectories exhibit a characteristic parabolic profile: initiating at a low magnitude, peaking within the intermediate transition zone (s = 1.4–1.8 m) (**Table 6**), and slightly attenuating toward the terminal boundary (s = 2.391 m). Specifically, during the incipient phase (s = 0–0.3 m), although the mechanical resistance (F_c) is at its maximum, P_{req} remains constrained to 3.4–3.6 kW due to the low initial translational velocity (u = 0.5 m/s). Notably, a kinematic anomaly occurs during this phase: P_{req} at θ = 10° exceeds that at θ = 20°. This is attributed to the more rapid draft attenuation on steeper gradients, which accelerates the decay of buoyancy and hydrodynamic drag; however, since P_{req} scales linearly with velocity, the superior acceleration rate at 10° overrides the resistive differential, yielding higher power demand. This underscores a unique hydro-terrestrial interaction where velocity and buoyancy effects temporarily supersede gravitational grade resistance.

Table 6. Maximum $P_{req}(s)$ power requirement (kW) in the intermediate zone.

Vehicle mass m (kg)	θ = 10°	θ = 15°	θ = 18°	θ = 20°
665	6.161	6.725	7.023	7.210
730	6.203	6.793	7.104	7.299
795	6.250	6.864	7.187	7.387
860	6.299	6.937	7.269	7.475

As the vehicle progresses into the intermediate region (s = 0.4–1.8 m), the hydrostatic buoyancy diminishes and grade resistance emerges as the dominant load, restoring the conventional relationship where steeper gradients necessitate higher power. The compounded effect of rising longitudinal velocity (u(s)) and substantial residual hydrodynamic drag (R(s)) drives $P_{req}(s)$ to its peak magnitude (**Table 5**). The maximum recorded demand of 7.475 kW (m = 860 kg, θ = 20°) approaches the nominal powertrain capacity (P_{motor} = 7.5 kW). Essentially, this peak load is required to sustain transient acceleration and overcome hydrodynamic surges during the transition, rather than for steady-state terrestrial cruising. These peak-power data establish a critical metric for assessing phase-transition gradeability and provide a robust foundation for energy management strategies and controller optimization in littoral environments.

3.3.5. Model validation discussion

Although full experimental validation—such as physical prototyping, towing tank tests, or Hardware-in-the-Loop (HIL) testing—remains a necessary phase for future work, the present study is strategically positioned at the preliminary design and theoretical framework development stage. To mitigate the absence of direct experimental data, the proposed simulation framework establishes its reliability through rigorous mathematical anchoring to well-validated empirical models. Specifically, the hydrodynamic resistance components during the in-water and transition phases are quantified using the Holtrop–Mennen method and ITTC standards. These established formulations are fundamentally derived from extensive statistical regression of historical towing tank test data for displacement hulls, thereby indirectly embedding empirical reliability into the analytical model. Similarly, the terrestrial traction and resistance forces are calculated based on conventional, experimentally validated longitudinal vehicle dynamics. By comparing the simulated trans-media dynamics with these standardized empirical frameworks, the proposed model demonstrated reasonable theoretical consistency. Furthermore, the smooth continuity observed in the velocity, resistance, buoyancy, and power profiles during the aquatic-to-terrestrial transition process (**Figures 14** and **15**) supports the numerical stability and physical plausibility of the mathematical framework. This pure numerical approach provides a crucial, cost-effective baseline for sizing the propulsion system and optimizing control algorithms before committing to capital-intensive physical prototyping.

3.3.6. Limitations and future research directions

The current model was created under idealized boundary conditions, assuming that the undersea environment is static and the on-land topography is smooth asphalt, based on the simulation findings and previously discussed topics. As a result, even though their impacts under actual operating conditions are known to be substantial, random external disturbances such as crosswinds, wave spectra, and hydrodynamic currents were not taken into account. The research team's next task is to create a control strategy for the hybrid propulsion system of the amphibious vehicles (AVs), building on the results of the initial mathematical model and the dynamic simulation results for the AVs on land, in water, and during the transition phase from water to land. The hybrid powertrain model for the amphibious vehicle will be used to estimate the vehicle range and energy efficiency both on land (according to speed cycles) and in water (at constant speed), with inputs including constant generator power and battery capacity, once the input parameters have been established. The ideal generator power and battery size will then be determined using a swarm-based optimization method so that the AVs can reach the necessary range as efficiently as possible. In order to finish the study and lay the groundwork for further research, experimental testing will be carried out to offer a strong basis for assessing and precisely drawing conclusions about the hybrid propulsion system.

4. Conclusion

Based on the suggested hybrid propulsion system (HEPS), this study created a dynamic simulation and mathematical model for an amphibious vehicle. The suggested hybrid powertrain was assessed and preliminary simulation results indicate satisfactory dynamic performance under the assumed operating conditions for the AVs when operating fully on land, in water, and during transitions from water to land through simulations carried out in the MATLAB/Simulink environment. Focusing purely on longitudinal dynamics, the simulation results show that the proposed HEPS configuration provides sufficient and continuous tractive effort to maintain dynamic continuity during inter-environment movement. The vehicle achieves the required on-road design speed of 60 km/h, reaches approximately 8.7 km/h in calm-water operation, and attains terminal transition velocities of approximately 7.2–9.5 km/h at the aquatic-to-terrestrial transition boundary. Furthermore, the results demonstrate that the amphibious vehicle's acceleration and directional stability during uphill travel meet the operational requirements when it transitions from water to land on a 20° incline in just 6.4 s.

Beyond theoretical modeling, these findings hold significant engineering application value for the commercial development of light-duty amphibious vehicles, particularly those deployed in ecotourism, flood rescue, and inland water patrol. For instance, the identification of the peak power demand (approximately 7.5 kW) occurring precisely in the intermediate transition zone serves as a critical boundary condition for engineers to correctly size the electric traction motor, define the battery pack's peak discharge capabilities, and design the thermal management system. Additionally, verifying that the vehicle can successfully clear a 20° incline in 6.4 s ensures that the proposed HEPS configuration is practically compatible with typical real-world infrastructure, such as standard boat slipways and natural riverbanks. Ultimately, by utilizing this unified parametric model, automotive engineers can rapidly evaluate gear ratios, payload distribution, and powertrain constraints during the preliminary design phase, substantially reducing the reliance on costly trial-and-error physical prototyping.

In line with the goals of intelligent and sustainable transportation solutions, these results offer a strong basis for further study and development of hybrid propulsion systems for amphibious vehicles (AVs). Future work will focus on improving the realism and applicability of the proposed framework by incorporating wave-induced disturbances, deformable soft-terrain interaction, CFD-enhanced hydrodynamic coupling, and experimental validation using prototype-based or Hardware-in-the-Loop (HIL) platforms. In addition, advanced control and energy-management strategies for hybrid amphibious propulsion systems will be investigated under more complex real-world operating conditions.

Author contributions: VTEN contributed to the conceptualization, methodology, software development, formal analysis, investigation, and preparation of the original draft. VTN contributed to the conceptualization, methodology, validation, formal analysis, manuscript review and editing, and supervision. THL contributed to the methodology, validation, and supervision. CTNN contributed to the conceptualization, methodology, software development, investigation, and data curation. TNV contributed to the methodology, software development, validation, investigation, resources, data curation, and visualization. All authors have read and agreed to the published version of the manuscript.

Funding: This work received no external funding.

Institutional review board statement: Not applicable.

Informed consent statement: Not applicable.

Data availability statement: The raw data supporting the conclusions of this article will be made available by the authors on request.

Acknowledgment: The authors would like to express their sincere gratitude to Ho Chi Minh City University of Technology and Engineering (HCM-UTE), Ho Chi Minh City University of Technology (HCMUT), and Nam Can Tho University (DNC) for their institutional support, research facilities, and valuable academic environment that enabled the successful completion of this study.

Conflict of interest: The authors declare no conflict of interest.

AI use statement: During the preparation of this manuscript, the authors used Gemini solely for language refinement. No AI tools were used for data analysis, interpretation, or generation of scientific content. All outputs were critically reviewed and edited by the authors. The authors take full responsibility for the integrity and accuracy of the work.

References

1. Zhang X, Huang J, Huang Y, et al. Intelligent amphibious ground-aerial vehicles: State of the art technology for future transportation. IEEE Transactions on Intelligent Vehicles. 2022; 8(1): 970–987.
2. Policarpo H, Lourenço JP, Anastácio AM, et al. Conceptual design of an unmanned electrical amphibious vehicle for ocean and land surveillance. World Electric Vehicle Journal. 2024; 15(7): 279.
3. Pan D, Xu X, Liu B, et al. A review on drag reduction technology: Focusing on amphibious vehicles. Ocean Engineering. 2023; 280: 114618.
4. Zou D, Jiao X, Zhou Y, et al. Design and multi-objective optimization of an electric inflatable pontoon amphibious vehicle. World Electric Vehicle Journal. 2025; 16(2): 58.
5. Luo H, Ding J, Jiang J, et al. Resistance characteristics and improvement of a pump-jet propelled wheeled

amphibious vehicle. Journal of Marine Science and Engineering. 2022; 10(8): 1092.
6. Liu B, Pan D, Xu X. Research on the resistance and maneuvering characteristics of an amphibious transport vehicle and the influence of stern hydrofoil. Ocean Engineering. 2024; 293: 116592.
7. Zhang Q, Jia B, Zhu Z, et al. Extreme Attitude Prediction of Amphibious Vehicles Based on Improved Transformer Model and Extreme Loss Function. Journal of Marine Science and Application. 2026; 25(1): 228–238.
8. Shang D, Zhang X, Liang F, et al. Optimization of Center of Gravity Position and Anti-Wave Plate Angle of Amphibious Unmanned Vehicle Based on Orthogonal Experimental Method. Computer Modeling in Engineering & Sciences. 2024; 139(2): 2027–2041.
9. Gan W, Zuo Z, Zhuang J, et al. Aerodynamic/Hydrodynamic Investigation of Water Cross-Over for a Bionic Unmanned Aquatic–Aerial Amphibious Vehicle. Biomimetics. 2024; 9(3): 181.
10. Jiang Z, Ding J, Li Z. Study on the Impact of Tail Wing Profiles on the Resistance Characteristics of Amphibious Vehicles. Journal of Marine Science and Engineering. 2024; 12(5): 780.
11. Jeong WJ, Nam S, Park JC, et al. Experimental and Numerical Study on Influence of Wheel Attachments on Resistance Performance of Amphibious Vessel for Marine Debris Collection. Journal of Marine Science and Engineering. 2024; 12(4): 570.
12. Xia M, Zhu Q, Yin Q, et al. Hydrodynamic simulation and experiment of a self-adaptive amphibious robot driven by tracks and bionic fins. Biomimetics. 2024; 9(10): 580.
13. Liu B, Xu X, Pan D, et al. Drag reduction design and research of high-speed amphibious vehicle’s deformable track wheels. Ships and Offshore Structures. 2023; 18(7): 970–979.
14. Pan D, Liu B, Xu X, et al. Experimental and CFD investigation on resistance reduction of hydrofoils for amphibious vehicles. Ships and Offshore Structures. 2024; 19(11): 1938–1951.
15. Shi Z, Tan X, Wang Y, et al. Experimental investigation of high speed cross-domain vehicles with hydrofoil. Journal of Marine Science and Engineering. 2023; 11(1): 152.
16. Yamashita H, Arnold A, Carrica PM, et al. Coupled multibody dynamics and computational fluid dynamics approach for amphibious vehicles in the surf zone. Ocean Engineering. 2022; 257: 111607.
17. Burciu Z, Kraskowski M, Gerigk M. Analysis of the process of water entry of an amphibious vehicle. Polish Maritime Research. 2012; 19(4): 5–14.
18. Huang B, Yuan Z, Yu W, et al. Driving Force Control for Water-to-Land Transition of Distributed Drive Amphibious Vehicles. SAE International; 2025. doi: 10.4271/2025-01-5011
19. Tison N. Amphibious Vehicle Water Egress Modeling and Simulation Using CFD and Wong’s Methodology. In: Proceedings of the Ground Vehicle Systems Engineering and Technology Symposium (GVSETS); 13–15 August 2019; Novi, MI, USA.
20. Liu B, Xu X, Pan D. Research on launching, water exiting, and river crossing of an amphibious vehicle. Physics of Fluids. 2023; 35(11): 113328. doi: 10.1063/5.0174148
21. Roh MI, Lee KY. Computational Ship Design. Springer; 2018.
22. Gillespie T. Fundamentals of Vehicle Dynamics. SAE International; 2021.
23. Larminie J, Lowry J. Electric Vehicle Technology Explained. John Wiley & Sons, Ltd.; 2012.
24. Ekinci S. A practical approach for design of marine propellers with systematic propeller series. Brodogradnja: An International Journal of Naval Architecture and Ocean Engineering for Research and Development. 2011; 62(2): 123–129.
25. Rajamani R. Vehicle Dynamics and Control. Springer; 2006.
26. Jazar RN. Vehicle Dynamics: Theory and Application. Springer Nature; 2025.